SIAM J. APPL. MATH.
Vol. 69, No. 6, pp. 1662–1681

DETECTING INCLUSIONS IN ELECTRICAL IMPEDANCE TOMOGRAPHY WITHOUT REFERENCE MEASUREMENTS*

BASTIAN HARRACH† AND JIN KEUN SEO‡

Abstract. We develop a new variant of the factorization method that can be used to detect inclusions in electrical impedance tomography from either absolute current-to-voltage measurements at a single, nonzero frequency or from frequency-difference measurements. This eliminates the need for numerically simulated reference measurements at an inclusion-free body and thus greatly improves the method's robustness against forward modeling errors, e.g., in the assumed body's shape.

Key words. inverse problems, electrical impedance tomography, complex conductivity, frequency-difference measurements, factorization method

AMS subject classifications. 35R30, 35Q60, 35J25, 35R05

DOI. 10.1137/08072142X

1. Introduction.

In electrical impedance tomography (EIT), we inject a time-harmonic current of I mA at a fixed angular frequency ω into an imaging subject using a pair of surface electrodes attached to its boundary. Then the induced time-harmonic electrical potential is dictated by the complex conductivity distribution σ^ω of the subject, the applied current, and the shape of the subject, where the real and imaginary part of the complex conductivity, $\Re(\sigma^\omega)$ and $\Im(\frac{\sigma^\omega}{\omega})$, are the real conductivity and the permittivity at the angular frequency ω, respectively. In EIT, we use measured boundary voltages generated by multiple injection currents to reconstruct an image of σ^ω inside the subject. It is well known that these boundary measurements are very insensitive and highly nonlinear to any local change of conductivity values away from the measuring points. Hence, the reconstructed image quality in terms of accuracy would be affected sensitively by unavoidable errors including the modeling errors and measurement noises.

Understanding the limited capabilities of static EIT imaging under realistic environments, numerous recent studies in EIT focus on the detection of conductivity anomalies instead of (e.g., cross-sectional) conductivity imaging; cf., e.g., [17, 21, 27, 28, 2, 9, 1, 20, 8, 15], the references therein, and the works connected with the factorization method cited further below.

Let us briefly explain the anomaly detection problem in EIT. Let the imaging object occupy a two- or three-dimensional region B with its smooth boundary ∂B, and let anomalies occupy a region Ω inside a background domain B of constant conductivity. We furthermore assume that the conductivity is isotropic. To distinguish the conductivity of the anomaly Ω and the surrounding homogeneous domain $B \setminus \Omega$, we denote the conductivity distribution at $\omega = 0$ by

$$\sigma(x) = \sigma_0 + \sigma_\Omega(x)\chi_\Omega(x),$$

*Received by the editors April 16, 2008; accepted for publication (in revised form) January 7, 2009; published electronically March 27, 2009.

http://www.siam.org/journals/siap/69-6/72142.html

†Birth name: Bastian Gebauer, Institut für Mathematik, Johannes Gutenberg-Universität, 55099 Mainz, Germany (harrach@math.uni-mainz.de). The work of this author was supported by the German Federal Ministry of Education and Research (BMBF) under grant 03HBPAM2, "Regularization techniques for electrical impedance tomography in medical and geological sciences".

‡Computational Science and Engineering, Yonsei University, Seoul, 120-749, Korea (seoj@yonsei.ac.kr). The work of this author was supported by WCU program R31-2008-000-10049-0.

where χ_Ω is the characteristic function of Ω and σ is a positive and bounded function in B. The inverse problem is to identify Ω from several pairs of Neumann-to-Dirichlet data

$$(g_j, \Lambda(g_j)) \in L^2_\diamond(\partial B) \times L^2_\diamond(\partial B), \quad j = 1, \ldots, L,$$

where $L^2_\diamond(\partial B) = \{\phi \in L^2(\partial B) \ : \ \int_{\partial B} \phi \, \mathrm{d}x = 0\}$. Here, $\Lambda(g) = u|_{\partial B}$ and u is the $H^1(B)$-solution for the Neumann boundary value problem:

$$\begin{aligned} \nabla \cdot (\sigma \nabla u) &= 0 \qquad \text{in } B, \\ \sigma \frac{\partial u}{\partial \nu}|_{\partial B} &= g, \qquad \int_{\partial B} u \, \mathrm{d}x = 0, \end{aligned}$$

where ν is the unit outward normal vector to the boundary ∂B.

One of the most successful EIT-methods for locating multiple anomalies would be the factorization method introduced by Kirsch [24] for inverse scattering problems and generalized to EIT-problems by Brühl and Hanke in [5, 4]; see also the recent book of Kirsch and Grinberg [26], the work of Kirsch [25] on the complex conductivity case, and [6, 14, 18, 11, 16, 19, 30, 13, 29] for further extensions of the method in the context of EIT. The factorization method is based on a characterization using the range of the difference between the Neumann-to-Dirichlet (NtD) map in the presence of anomalies and that in the absence of anomalies: $z \in \Omega$ if and only if $\Phi_z|_{\partial B}$ is in the range of the operator $|\Lambda - \Lambda_0|^{1/2}$, where Λ_0 is the NtD map corresponding to the reference homogeneous conductivity $\sigma(x) = \sigma_0$ and $\Phi_z(x)$ is the solution of

$$\Delta_x \Phi_z(x) = d \cdot \nabla_x \delta_z(x) \quad \text{in } B, \quad \frac{\partial}{\partial \nu} \Phi_z|_{\partial \Omega} = 0, \quad \text{and} \quad \int_{\partial B} \Phi_z(x) \, \mathrm{d}x = 0,$$

where d is any unit vector and δ_z is the Dirac delta function at z.

For the practical application of the factorization method for static EIT systems, the requirement of the reference NtD data Λ_0 is a drawback. While, in practice, a rough approximation of the NtD map Λ can be obtained from the current-to-voltage data, the corresponding current-to-voltage data for the reference NtD map Λ_0 in the absence of anomalies is usually not available.

Hence, one uses numerically simulated data corresponding to Λ_0 by solving the forward problem $\nabla \cdot (\sigma_0 \nabla u) = 0$ in B with mimicked Neumann data representing the injection current in the EIT system. Noting that the simulated Dirichlet data is mainly depending on the geometry of ∂B and the Neumann data, instead of the conductivity σ_0 (which acts merely as a scaling factor), the requirement of the reference NtD data Λ_0 makes the factorization method very sensitive to forward modeling errors including the boundary geometry error and electrodes position uncertainty (related to the mimicked Neumann data), since its image reconstruction problem is ill-posed. Hence, it is desirable to eliminate the requirement of the reference NtD data Λ_0.

In this work, we adopt the frequency-difference EIT system [31, 32] to obtain a subsidiary NtD data Λ_ω at a fixed angular frequency ω taken from the range of $1\text{kHz} \leq \frac{\omega}{2\pi} \leq 500\text{kHz}$. $\Lambda_\omega(g)$ is the Dirichlet data of the complex potential u_ω which satisfies

$$\nabla \cdot (\sigma^\omega \nabla u_\omega) = 0 \quad \text{in } B, \quad \sigma^\omega \frac{\partial}{\partial \nu} u_\omega|_{\partial B} = g, \quad \text{and} \quad \int_{\partial B} u_\omega \, \mathrm{d}x = 0.$$

Our aim is to substitute Λ_ω for Λ_0 in the conventional factorization method and use an interrelation between Λ and Λ_ω to locate the anomalies Ω. However, due to

$\Im\{\sigma^\omega\} \neq 0$, the operator Λ_ω is not self-adjoint and $\Lambda - \Lambda_\omega$ is neither semipositive nor seminegative.

In this work, we show that, for an arbitrary fixed nonzero frequency ω, both, the imaginary part of $\sigma_0^\omega \Lambda_\omega$ and the real part of the normalized difference $\sigma_0 \Lambda - \sigma_0^\omega \Lambda_\omega$ (or actually any other normalized difference of measurements taken at two different frequencies), provide a constructive way of locating Ω, where σ_0^ω is the background complex conductivity at the angular frequency ω. To our knowledge this is the first characterization result that works without reference measurements. We numerically demonstrate that the proposed new variant of the factorization method locates successfully the region Ω with a reasonable accuracy in the presence of boundary geometry errors and measurement noise. We also describe a heuristic approach to estimate an unknown background conductivity from the measured data and numerically test it on a homogeneous, as well as on a slightly inhomogeneous, background.

In section 2 we formulate and prove our main results. In section 3 we test our method numerically, compare its sensitivity to body shape errors with the conventional factorization method, and describe a heuristic approach to estimate an unknown background conductivity. Section 4 contains some concluding remarks.

2. Characterization of an inclusion without reference data. Let $B \subset \mathbb{R}^n$, $n \geq 2$, be a smoothly bounded domain describing the investigated body. Let $\omega > 0$ be an arbitrary fixed frequency and denote by σ^ω the body's complex conductivity at some fixed nonzero frequency $\omega > 0$. We assume that $\Re(\sigma^\omega) \in L^\infty_+(B;\mathbb{R})$ and $\Im(\sigma^\omega) \in L^\infty(B;\mathbb{R})$, where $\Re(\cdot)$ and $\Im(\cdot)$ denote the real and imaginary part, the subscript "+" indicates functions with positive (essential) infima, and throughout this work all function spaces consist of complex valued functions if not stated otherwise.

A time-harmonic current with (complex) amplitude $g \in L^2_\diamond(\partial B)$ and frequency ω that is applied to the body's surface gives rise to an electric potential $u_\omega \in H^1(B)$ that satisfies

$$\nabla \cdot (\sigma^\omega \nabla u_\omega) = 0 \quad \text{in } B \quad \text{and} \quad \sigma^\omega \partial_\nu u_\omega|_{\partial B} = g, \tag{2.1}$$

where $L^2_\diamond(\partial B)$ is the subspace of $L^2(\partial B)$-functions with vanishing integral mean, ν is the outer normal on ∂B.

It is a well-known consequence of the Lax–Milgram theorem (cf., e.g., [7, Chapter VI, §3, Theorem 7]) that there exists a solution of (2.1) and that this solution is uniquely determined up to addition of a constant function. We denote the quotient space of $H^1(B)$ modulo constant functions by $H^1_\diamond(B)$. The trace operator $v \mapsto v|_{\partial B}$ canonically extends to $H^1_\diamond(B) \to L^2(\partial B)/\mathbb{C}$, where we identify the latter space with $L^2_\diamond(\partial B)$ by appropriately fixing the ground level.

The inverse problem of frequency-dependent EIT is the problem of determining (properties of) σ^ω from measuring one or several pairs of Neumann and Dirichlet boundary values $(u_\omega|_{\partial B}, \sigma^\omega \partial_\nu u_\omega|_{\partial B})$. Mathematically, the knowledge of all such pairs is equivalent to knowing the Neumann-to-Dirichlet operator

$$\Lambda_\omega : L^2_\diamond(\partial B) \to L^2_\diamond(\partial B), \quad g \mapsto u_\omega|_{\partial B},$$

where u_ω solves (2.1). It is easily checked that Λ_ω is linear and compact.

2.1. The main results. In this work, we assume that the conductivity of the body is constant outside one or several inclusions, i.e.,

$$\sigma^\omega(x) = \sigma_0^\omega + \sigma_\Omega^\omega(x)\chi_\Omega(x),$$

where Ω is some open (possibly disconnected) set with smooth boundary and connected complement, $\overline{\Omega} \subset B$, and $\sigma_0^\omega \in \mathbb{C}$, $\sigma_\Omega^\omega \in L^\infty(\Omega)$ are such that $\Re(\sigma^\omega) \in L_+^\infty(B;\mathbb{R})$.

We will show that the inclusion Ω can be determined from the Neumann-to-Dirichlet operator Λ_ω using the same singular dipole potentials that were introduced for the factorization method by Brühl and Hanke in [5, 4]. For an arbitrary direction $d \in \mathbb{R}^n$, $|d| = 1$, and every point $z \in B$, let Φ_z be the solution of

$$\Delta_x \Phi_z(x) = d \cdot \nabla_x \delta_z(x) \quad \text{in } B$$

with homogeneous Neumann boundary values $\partial_\nu \Phi_z(x)|_{\partial B} = 0$ and vanishing integral mean on ∂B.

THEOREM 2.1. *Assume that either*

$$\Im\left(\frac{\sigma_\Omega^\omega}{\sigma_0^\omega}\right) \in L_+^\infty(\Omega;\mathbb{R}) \quad \text{or} \quad -\Im\left(\frac{\sigma_\Omega^\omega}{\sigma_0^\omega}\right) \in L_+^\infty(\Omega;\mathbb{R}). \tag{2.2}$$

Then

$$z \in \Omega \quad \text{if and only if} \quad \Phi_z|_{\partial B} \in \mathcal{R}\left(\left|\Im\left(\sigma_0^\omega \Lambda_\omega\right)\right|^{1/2}\right),$$

where the imaginary part of a bounded linear operator $A \in \mathcal{L}(H)$ on a complex Hilbert space H is defined by $\Im(A) := \frac{1}{2\mathrm{i}}(A - A^*)$, and $\mathcal{R}(A)$ denotes the range of A.

We also show a complementary result for the real part of frequency-difference data. Let $0 \le \tau \ne \omega$ be another fixed frequency (possibly being zero) for which the body's complex conductivity is σ^τ, with $\Re(\sigma^\tau) \in L_+^\infty(B;\mathbb{R})$. We assume that σ^τ is also constant outside the same inclusion Ω, i.e., $\sigma^\tau = \sigma_0^\tau + \sigma_\Omega^\tau(x)\chi_\Omega(x)$ with $\sigma_0^\tau \in \mathbb{C}$. Measurements at the frequency τ are described by the NtD operator Λ_τ which is defined analogously to Λ_ω.

THEOREM 2.2. *If either*

$$\Re\left(\frac{\sigma_\Omega^\tau}{\sigma_0^\tau}\right) - \Re\left(\frac{\sigma_\Omega^\omega}{\sigma_0^\omega}\right) - \frac{\Im\left(\frac{\sigma_\Omega^\omega}{\sigma_0^\omega}\right)^2}{\Re\left(\frac{\sigma^\omega}{\sigma_0^\omega}\right)} \in L_+^\infty(\Omega;\mathbb{R}), \tag{2.3}$$

or

$$\Re\left(\frac{\sigma_\Omega^\omega}{\sigma_0^\omega}\right) - \Re\left(\frac{\sigma_\Omega^\tau}{\sigma_0^\tau}\right) - \frac{\Im\left(\frac{\sigma_\Omega^\tau}{\sigma_0^\tau}\right)^2}{\Re\left(\frac{\sigma^\tau}{\sigma_0^\tau}\right)} \in L_+^\infty(\Omega;\mathbb{R}), \tag{2.4}$$

then

$$z \in \Omega \quad \text{if and only if} \quad \Phi_z|_{\partial B} \in \mathcal{R}\left(\left|\Re\left(\sigma_0^\omega \Lambda_\omega - \sigma_0^\tau \Lambda_\tau\right)\right|^{1/2}\right),$$

where the real part of a bounded linear operator $A \in \mathcal{L}(H)$ on a complex Hilbert space H is defined by $\Re(A) := \frac{1}{2}(A + A^*)$.

Before we prove these two theorems in the next subsection, let us comment on their relevance. In contrast to the conventional factorization method where the measured NtD data is compared to reference data that is usually not available by experiment (with the disadvantages described in the introduction), both theorems use only experimentally available NtD measurements. Our theorems require NtD data either

at just one (nonzero) frequency, which is then compared to its own adjoint (Theorem 2.1) or NtD data measured at two different frequencies (possibly one being zero), which are then compared to each other (Theorem 2.2). In particular, this means that we can replace unavailable reference measurements in the conventional factorization methods by experimentally available measurements at an arbitrary nonzero frequency, which strongly reduces the methods sensitivity to boundary geometry errors as we will demonstrate numerically in section 3. In practice, one may have access to measurements at more than two frequencies. This redundancy can surely be used to further increase the performance or robustness of our method, but we have not studied this question in detail.

The assumptions (2.2)–(2.4) are arguably not very intuitive. For the practically relevant model case that the real conductivity $\kappa = \Re(\sigma^\omega)$ and the permittivity $\epsilon = \Im(\frac{\sigma^\omega}{\omega})$ are not frequency-dependent, they can be restated as follows.

Remark 2.3. Let

$$\sigma^\tau(x) = \kappa(x) + \mathrm{i}\tau\epsilon(\mathrm{x}), \qquad \kappa(x) = \kappa_0 + \kappa_\Omega(x)\chi_\Omega(x),$$
$$\sigma^\omega(x) = \kappa(x) + \mathrm{i}\omega\epsilon(\mathrm{x}), \qquad \epsilon(x) = \epsilon_0 + \epsilon_\Omega(x)\chi_\Omega(x),$$

with $\kappa_0, \epsilon_0 \in \mathbb{R}$, $\kappa_\Omega, \epsilon_\Omega \in L^\infty(\Omega;\mathbb{R})$. Then

$$\Im\left(\frac{\sigma^\omega_\Omega}{\sigma^\omega_0}\right) = \frac{\omega}{\kappa_0^2 + \omega^2\epsilon_0^2}(\kappa_0\epsilon_\Omega - \kappa_\Omega\epsilon_0),$$

$$\Re\left(\frac{\sigma^\tau_\Omega}{\sigma^\tau_0}\right) - \Re\left(\frac{\sigma^\omega_\Omega}{\sigma^\omega_0}\right) - \frac{\Im\left(\frac{\sigma^\omega_\Omega}{\sigma^\omega_0}\right)^2}{\Re\left(\frac{\sigma^\omega}{\sigma^\omega_0}\right)} = \frac{(\kappa_0\epsilon_\Omega - \kappa_\Omega\epsilon_0)(\tau^2\kappa\epsilon_0 - \omega^2\kappa_0\epsilon)}{(\kappa_0^2 + \tau^2\epsilon_0^2)(\kappa_0\kappa + \omega^2\epsilon_0\epsilon)},$$

and the same identities hold with ω and τ interchanged. Hence, (2.2) is equivalent to

$$\kappa_0\epsilon_\Omega - \kappa_\Omega\epsilon_0 \in L^\infty_+(\Omega;\mathbb{R}) \quad \text{or} \quad \kappa_\Omega\epsilon_0 - \kappa_0\epsilon_\Omega \in L^\infty_+(\Omega;\mathbb{R}). \tag{2.5}$$

If ω is sufficiently larger than τ, then (2.5) is also equivalent to the disjunction of (2.3) and (2.4). For $\tau = 0$, every $\omega > 0$ is sufficiently large.

In particular, our method can identify inclusions where only the real conductivity or only the permittivity differs from the background, and this deviance is of the same sign in all inclusions. However, there exist combinations where a jump κ_Ω in the real conductivity and a jump ϵ_Ω in the permittivity cancel each other out, in the sense that

$$\kappa_0\epsilon_\Omega - \kappa_\Omega\epsilon_0 = 0.$$

Inclusions with this property cannot be detected by our method. In fact, they are completely invisible to weighted frequency-difference measurements, as one easily checks that in this case

$$\Im\left(\sigma_0^\omega\Lambda_\omega\right) = 0 \quad \text{and} \quad \Re\left(\sigma_0^\omega\Lambda_\omega - \sigma_0^\tau\Lambda_\tau\right) = 0.$$

There is also another drawback in our method compared to the original factorization method. The original method also works in the case of an inhomogeneous (but known) background medium, which only requires the replacement of the singular dipole potentials Φ_z by the corresponding dipole potentials in the inhomogeneous

background. For our method this is not sufficient, since we also need the constant background conductivities to form the weighted differences of the NtD data. Hence, up to now, our method can only be applied to a homogeneous (constant) background medium. We believe, however, that our results cover the most relevant case in practice, where no accurate information about the background is available (except of being "almost constant"), and we describe in subsection 3.3 a heuristic approach how even an unknown background value can be estimated from the measured data. Our numerical results indicate that this approach still yields reasonable results if the unknown background is slightly inhomogeneous.

2.2. Proof of the main results. We start with some notations. The inner product on a complex Hilbert space H is denoted by $(\cdot,\cdot)$ and the pairing on H and its antidual H' is denoted by $\langle\cdot,\cdot\rangle_{H'\times H}$. Both are ordered in the way that they are linear in the first and antilinear in their second argument. For an operator $A \in \mathcal{L}(H_1, H_2)$ acting between Hilbert spaces H_1 and H_2, we rigorously distinguish between the dual operator $A' \in \mathcal{L}(H_2', H_1')$ and the adjoint operator $A^* \in \mathcal{L}(H_2, H_1)$.

Analogously to the definition of $H^1_\diamond(B)$, we denote by $H^1_\diamond(B \setminus \overline{\Omega})$, $H^1_\diamond(\Omega)$, and $H^{1/2}_\diamond(\partial\Omega)$ the quotient spaces of $H^1(B \setminus \overline{\Omega})$, $H^1(\Omega)$, and of the the trace space $H^{1/2}(\partial\Omega)$ modulo locally constant functions. (Thus, for disconnected Ω a multidimensional space is factored out.) The antidual of $H^{1/2}_\diamond(\partial\Omega)$ is denoted by $H^{-1/2}_\diamond(\partial\Omega)$, and we identify $L^2_\diamond(\partial B)$ with its antidual.

We will prove both results using a factorization of the difference of $\sigma_0^\omega\Lambda_\omega$ and the reference NtD operator Λ_0 corresponding to a constant conductivity equal to one, i.e.,

$$\Lambda_0 :\ L^2_\diamond(\partial B) \to L^2_\diamond(\partial B), \quad g \mapsto u_0|_{\partial B},$$

where u solves

$$\Delta u_0 = 0 \quad \text{in } B \quad \text{and} \quad \partial_\nu u_0|_{\partial B} = g.$$

It is well known and easily checked that Λ_0 is linear, compact, and self-adjoint. Let us stress again that we only require measurements at one arbitrary fixed frequency $\omega > 0$ (for Theorem 2.1), or at two arbitrary, but different, fixed frequencies $\omega > 0$, $\tau \geq 0$ (for Theorem 2.2). Λ_0 merely serves as an auxiliary operator that will cancel out later in our proof. Unlike other applications of the factorization method, Λ_0 does not have to correspond to real measurements.

For the factorization we also introduce the operator

$$L :\ H^{-1/2}_\diamond(\partial\Omega) \to L^2_\diamond(\partial B), \quad \psi \mapsto w|_{\partial B},$$

where $w \in H^1_\diamond(B \setminus \overline{\Omega})$ solves

$$\Delta w = 0, \qquad \partial_\nu w|_{\partial B} = 0, \qquad \partial_\nu w^+|_{\partial\Omega} = -\psi,$$

with ν being the normal on $\partial\Omega$ oriented into $B\setminus\overline{\Omega}$ and we denote by the superscripts "+", resp., "−" that the trace is taken from $B\setminus\overline{\Omega}$ and Ω, respectively. We also define

$$F_0 :\ H^{1/2}_\diamond(\partial\Omega) \to H^{-1/2}_\diamond(\partial\Omega), \qquad F_0\phi = \partial_\nu v_0^+|_{\partial\Omega},$$

$$F_\omega :\ H^{1/2}_\diamond(\partial\Omega) \to H^{-1/2}_\diamond(\partial\Omega), \qquad F_\omega\phi = \partial_\nu v_\omega^+|_{\partial\Omega},$$

where $v_0, v_\omega \in H^1_\diamond(B \setminus \partial\Omega)$ solve

$$\Delta v_0 = 0 \quad \text{in } B \setminus \partial\Omega, \qquad \nabla \cdot \frac{\sigma^\omega}{\sigma_0^\omega} \nabla v_\omega = 0 \quad \text{in } B \setminus \partial\Omega,$$

$$\partial_\nu v_0|_{\partial B} = 0, \qquad \partial_\nu v_\omega|_{\partial B} = 0,$$

$$[v_0]_{\partial\Omega} = \phi, \qquad [v_\omega]_{\partial\Omega} = \phi,$$

$$[\partial_\nu v_0]_{\partial\Omega} = 0, \qquad \left[\frac{\sigma^\omega}{\sigma_0^\omega} \partial_\nu v_\omega\right]_{\partial\Omega} = 0,$$

with $[\cdot]$ denoting the difference of the trace taken from $B \setminus \overline{\Omega}$ minus the trace taken from Ω. (Note that one easily checks that F_0 and F_ω are indeed well defined on these spaces.)

For the case of frequency-difference data, we also define F_τ analogously to F_ω. For the sake of readability we formulate the next two lemmas only for the frequency ω, though they just as well hold for τ.

LEMMA 2.4. *The difference of the Neumann-to-Dirichlet operators can be factorized into*

$$\Lambda_0 - \sigma_0^\omega \Lambda_\omega = L(F_0 - F_\omega)L'.$$

Proof. We proceed similarly to [10]. For given $g \in H_\diamond^{-\frac{1}{2}}(\partial B)$ let $\tilde{w} \in H^1_\diamond(B \setminus \overline{\Omega})$ solve

$$\Delta \tilde{w} = 0 \quad \text{in } B \setminus \overline{\Omega} \quad \text{and} \quad \partial_\nu \tilde{w} = \begin{cases} 0 & \text{on } \partial\Omega, \\ g & \text{on } \partial B. \end{cases}$$

Let $\psi \in H_\diamond^{-\frac{1}{2}}(\partial\Omega)$ and $w \in H^1_\diamond(B \setminus \overline{\Omega})$ be the function from the definition of $L\psi$. Then

$$\langle \psi, L'g \rangle = \overline{\langle g, L\psi \rangle} = \overline{\langle \partial_\nu \tilde{w}|_{\partial B}, w|_{\partial B} \rangle} = \int_{B \setminus \overline{\Omega}} \overline{\nabla \tilde{w}} \cdot \nabla w \, \mathrm{d}x = \left\langle -\partial_\nu w^+|_{\partial\Omega}, \tilde{w}^+|_{\partial\Omega} \right\rangle$$

$$= \left\langle \psi, \tilde{w}^+|_{\partial\Omega} \right\rangle,$$

and thus $L'g = \tilde{w}^+|_{\partial\Omega}$.

Now let $v_0, v_\omega \in H^1_\diamond(B \setminus \partial\Omega)$ be the solutions from the definition of $F_0\tilde{w}^+|_{\partial\Omega}$, resp., $F_\omega \tilde{w}^+|_{\partial\Omega}$. We define $u_0, u_\omega \in H^1_\diamond(B \setminus \partial\Omega)$ by setting $u_0 = -v_0$, resp., $u_\omega = -v_\omega$ on Ω and $u_0 = \tilde{w} - v_0$, resp., $u_\omega = \tilde{w} - v_\omega$ on $B \setminus \overline{\Omega}$. Then $u_0, \frac{1}{\sigma_0^\omega} u_\omega \in H^1_\diamond(B)$ and they solve the equations in the definitions of $\Lambda_0 g$ and $\Lambda_\omega g$. Thus,

$$(\Lambda_0 - \sigma_0^\omega \Lambda_\omega)g = (u_0 - u_\omega)|_{\partial B} = -(v_0 - v_\omega)|_{\partial B}.$$

Since $\Delta(v_0 - v_\omega) = 0$ in $B \setminus \overline{\Omega}$ and $\partial_\nu(v_0 - v_\omega)|_{\partial B} = 0$, we also have

$$L(\partial_\nu(v_0^+ - v_\omega^+)|_{\partial\Omega}) = -(v_0 - v_\omega)|_{\partial B},$$

and thus

$$(\Lambda_0 - \sigma_0^\omega \Lambda_\omega)g = L(\partial_\nu(v_0^+ - v_\omega^+)|_{\partial\Omega}) = L(F_0 - F_\omega)\tilde{w}^+|_{\partial\Omega} = L(F_0 - F_\omega)L'g. \qquad \square$$

LEMMA 2.5. *For given $\phi \in H^{1/2}_\diamond(\partial\Omega)$ let $v_0, v_\omega \in H^1_\diamond(B \setminus \partial\Omega)$ be the solutions in the definition of F_0, F_ω and let $v_\phi \in H^1(B \setminus \partial\Omega)$ be such that $v_\phi^+|_{\partial\Omega} = \phi$ and $v_\phi|_\Omega = 0$. Set $\tilde{v}_0 := v_0 - v_\phi$ and $\tilde{v}_\omega := v_\omega - v_\phi$. Then*

$$\langle (F_0 - F_\omega)\phi, \phi\rangle = \int_B |\nabla \tilde{v}_0|^2 \,\mathrm{d}x - \int_B \frac{\overline{\sigma^\omega}}{\overline{\sigma_0^\omega}} |\nabla \tilde{v}_\omega|^2 \,\mathrm{d}x.$$

Furthermore, there exists a constant $c_\omega > 0$ such that

$$\int_\Omega |\nabla \tilde{v}_\omega|^2 \,\mathrm{d}x = \int_\Omega |\nabla v_\omega|^2 \,\mathrm{d}x \geq c_\omega \|\phi\|^2 \quad \text{for all } \phi \in H^{1/2}_\diamond(\partial\Omega).$$

Proof. One easily checks that the functions $\tilde{v}_0, \tilde{v}_\omega \in H^1_\diamond(B)$ solve

$$\int_B \nabla \tilde{v}_0 \cdot \overline{\nabla w} \,\mathrm{d}x = -\int_{B\setminus\Omega} \nabla v_\phi \cdot \overline{\nabla w} \,\mathrm{d}x, \tag{2.6}$$

$$\int_B \frac{\sigma^\omega}{\sigma_0^\omega} \nabla \tilde{v}_\omega \cdot \overline{\nabla w} \,\mathrm{d}x = -\int_{B\setminus\Omega} \nabla v_\phi \cdot \overline{\nabla w} \,\mathrm{d}x \tag{2.7}$$

for all $w \in H^1_\diamond(B)$. Thus, we obtain

$$\begin{aligned}
\langle (F_0 - F_\omega)\phi, \phi\rangle &= \langle \partial_\nu v_0^+|_{\partial\Omega}, \phi\rangle - \langle \partial_\nu v_\omega^+|_{\partial\Omega}, \phi\rangle \\
&= \int_{B\setminus\overline{\Omega}} \nabla v_\omega \cdot \overline{\nabla v_\phi} \,\mathrm{d}x - \int_{B\setminus\overline{\Omega}} \nabla v_0 \cdot \overline{\nabla v_\phi} \,\mathrm{d}x \\
&= \int_{B\setminus\overline{\Omega}} \nabla \tilde{v}_\omega \cdot \overline{\nabla v_\phi} \,\mathrm{d}x - \int_{B\setminus\overline{\Omega}} \nabla \tilde{v}_0 \cdot \overline{\nabla v_\phi} \,\mathrm{d}x \\
&= \int_B |\nabla \tilde{v}_0|^2 \,\mathrm{d}x - \int_B \overline{\left(\frac{\sigma^\omega}{\sigma_0^\omega}\right)} |\nabla \tilde{v}_\omega|^2 \,\mathrm{d}x.
\end{aligned}$$

To prove the second assertion we first note that the Neumann boundary values

$$F_\omega \phi = \partial_\nu v_\omega^+|_{\partial\Omega} = \frac{\sigma^\omega}{\sigma_0^\omega} \partial_\nu v_\omega^-|_{\partial\Omega}$$

depend continuously on $v_\omega|_\Omega = \tilde{v}_\omega|_\Omega \in H^1_\diamond(\Omega)$, so that there exists $c'_\omega > 0$ such that

$$\int_\Omega |\nabla \tilde{v}_\omega|^2 \,\mathrm{d}x = \int_\Omega |\nabla v_\omega|^2 \,\mathrm{d}x \geq c'_\omega \|F_\omega \phi\|^2 \quad \text{for all } \phi \in H^{1/2}_\diamond(\partial\Omega).$$

Thus, it only remains to show that F_ω is bijective. Its injectivity is obvious and its surjectivity is shown as in the proof of [10, Lemma 3.3] by checking that a right inverse of F_ω is given by $-\lambda^\omega_{B\setminus\overline{\Omega}} - \lambda^\omega_\Omega$, where λ^ω_Ω and $\lambda^\omega_{B\setminus\overline{\Omega}}$ are the NtD operators on the inclusion Ω, resp., on its complement $B \setminus \overline{\Omega}$. ∎

LEMMA 2.6. *The assumptions of Theorem* 2.1 *imply that there exist $c, C > 0$ such that*

$$c\|L'g\|^2 \leq (|\Im(\sigma_0^\omega \Lambda_\omega)|\, g, g) \leq C\|L'g\|^2. \tag{2.8}$$

For the case of frequency-difference data, the assumptions of Theorem 2.2 *imply that there exist* $c', C' > 0$ *such that*

$$c' \|L'g\|^2 \leq (|\Re(\sigma_0^\omega \Lambda_\omega - \sigma_0^\tau \Lambda_\tau)| g, g) \leq C' \|L'g\|^2. \tag{2.9}$$

Proof. For every $g \in L^2_\diamond(\partial B)$, $\phi := L'g$, let $\tilde{v}_\omega, v_\phi$ be the functions defined in Lemma 2.5. Noting that $\Lambda_0 = \Lambda_0'$ and $F_0 = F_0'$, we obtain from Lemmas 2.4 and 2.5 that

$$\begin{aligned}(\Im(\sigma_0^\omega \Lambda_\omega) g, g) &= \langle \Im(F_\omega) L'g, L'g \rangle \\ &= \frac{1}{2\mathrm{i}} \left(\langle (F_\omega - F_0)\phi, \phi \rangle - \overline{\langle (F_\omega - F_0)\phi, \phi \rangle} \right) \\ &= -\int_B \Im\left(\frac{\sigma^\omega}{\sigma_0^\omega}\right) |\nabla \tilde{v}_\omega|^2 \, \mathrm{d}x = -\int_\Omega \Im\left(\frac{\sigma_\Omega^\omega}{\sigma_0^\omega}\right) |\nabla \tilde{v}_\omega|^2 \, \mathrm{d}x.\end{aligned}$$

Hence, $|\Im(\sigma_0^\omega \Lambda_\omega)|$ is either $\Im(\sigma_0^\omega \Lambda_\omega)$ or $-\Im(\sigma_0^\omega \Lambda_\omega)$, the lower bound in assertion (2.8) follows from Lemma 2.5, and the upper bound follows from the the continuity of F_ω.

To prove the second assertion for the case of frequency-difference data, let $\tilde{v}_\tau$ be defined analogously to $\tilde{v}_\omega$. We now proceed similar to Ide et al. [20, Lemma 2.6]; cf. also the similar arguments in Kang, Seo, and Sheen [23] and Kirsch [25]. Using (2.7) and its analog for the frequency τ, we derive

$$\begin{aligned}0 &\leq \int_B \Re\left(\frac{\sigma^\tau}{\sigma_0^\tau}\right) \left| \nabla \tilde{v}_\tau - \frac{\frac{\sigma^\omega}{\sigma_0^\omega}}{\Re\left(\frac{\sigma^\tau}{\sigma_0^\tau}\right)} \nabla \tilde{v}_\omega \right|^2 \, \mathrm{d}x \\ &= \int_B \Re\left(\frac{\sigma^\tau}{\sigma_0^\tau}\right) |\nabla \tilde{v}_\tau|^2 \, \mathrm{d}x - 2\Re\left(\int_B \frac{\sigma^\omega}{\sigma_0^\omega} \nabla \tilde{v}_\omega \cdot \overline{\nabla \tilde{v}_\tau} \, \mathrm{d}x \right) + \int_B \frac{\left|\frac{\sigma^\omega}{\sigma_0^\omega}\right|^2}{\Re\left(\frac{\sigma^\tau}{\sigma_0^\tau}\right)} |\nabla \tilde{v}_\omega|^2 \, \mathrm{d}x \\ &= -\int_B \Re\left(\frac{\sigma^\tau}{\sigma_0^\tau}\right) |\nabla \tilde{v}_\tau|^2 \, \mathrm{d}x + \int_B \frac{\left|\frac{\sigma^\omega}{\sigma_0^\omega}\right|^2}{\Re\left(\frac{\sigma^\tau}{\sigma_0^\tau}\right)} |\nabla \tilde{v}_\omega|^2 \, \mathrm{d}x.\end{aligned}$$

Thus, it follows from Lemmas 2.4 and 2.5 that

$$\begin{aligned}&(\Re(\sigma_0^\omega \Lambda_\omega - \sigma_0^\tau \Lambda_\tau) g, g) \\ &= \int_B \Re\left(\frac{\sigma^\omega}{\sigma_0^\omega}\right) |\nabla \tilde{v}_\omega|^2 \, \mathrm{d}x - \int_B \Re\left(\frac{\sigma^\tau}{\sigma_0^\tau}\right) |\nabla \tilde{v}_\tau|^2 \, \mathrm{d}x \\ &\geq \int_B \left(\Re\left(\frac{\sigma^\omega}{\sigma_0^\omega}\right) - \frac{\left|\frac{\sigma^\omega}{\sigma_0^\omega}\right|^2}{\Re\left(\frac{\sigma^\tau}{\sigma_0^\tau}\right)} \right) |\nabla \tilde{v}_\omega|^2 \, \mathrm{d}x \\ &= \int_\Omega \frac{\Re\left(\frac{\sigma^\omega}{\sigma_0^\omega}\right)}{\Re\left(\frac{\sigma^\tau}{\sigma_0^\tau}\right)} \left(\Re\left(\frac{\sigma_\Omega^\tau}{\sigma_0^\tau}\right) - \Re\left(\frac{\sigma_\Omega^\omega}{\sigma_0^\omega}\right) - \frac{\Im\left(\frac{\sigma_\Omega^\omega}{\sigma_0^\omega}\right)^2}{\Re\left(\frac{\sigma^\omega}{\sigma_0^\omega}\right)} \right) |\nabla \tilde{v}_\omega|^2 \, \mathrm{d}x.\end{aligned}$$

Using $\Re\left(\frac{\sigma^\omega}{\sigma_0^\omega}\right), \Re\left(\frac{\sigma^\tau}{\sigma_0^\tau}\right) \in L_+^\infty(B)$, and assumption (2.3), we obtain a $c'' > 0$ with

$$(\Re\left(\sigma_0^\omega \Lambda_\omega - \sigma_0^\tau \Lambda_\tau\right) g, g) \geq c'' \int_\Omega |\nabla \tilde{v}_\omega|^2 \, \mathrm{d}x.$$

An analog equation follows from interchanging ω and τ and using assumption (2.4). Hence, if either (2.3) or (2.4) holds, then $|\Re\left(\sigma_0^\omega \Lambda_\omega - \sigma_0^\tau \Lambda_\tau\right)|$ is either $\Re\left(\sigma_0^\omega \Lambda_\omega - \sigma_0^\tau \Lambda_\tau\right)$ or $\Re\left(\sigma_0^\tau \Lambda_\tau - \sigma_0^\omega \Lambda_\omega\right)$, and in both cases the lower bound in assertion (2.9) follows from Lemma 2.5. The upper bound in assertion (2.9) follows from the factorization in Lemma 2.4 and the continuity of F_ω and F_τ. ∎

We also need two known lemmas from previous applications of the factorization method. The first one relates the range of an operator to the norm of its dual or adjoint and the second one shows that the inclusion Ω can be determined from $\mathcal{R}(L)$.

LEMMA 2.7. *Let H_i, $i = 1, 2$, be two Hilbert spaces with norms $\|\cdot\|_i$, X be a third Hilbert space, and $A_i \in \mathcal{L}(X, H_i)$.*

If $\|A_1 x\|_1 \leq \|A_2 x\|_2$ for all $x \in X$, then $\mathcal{R}(A_1^*) \subseteq \mathcal{R}(A_2^*)$ and $\mathcal{R}(A_1') \subseteq \mathcal{R}(A_2')$.

Proof. This follows from the so-called "14th important property of Banach spaces" in Bourbaki [3]; cf. also [10, Lemma 3.4, Cor. 3.5] for an elementary proof for real spaces that holds as well in this complex case. ∎

LEMMA 2.8. *$\Phi_z|_{\partial B} \in \mathcal{R}(L)$ if and only if $z \in \Omega$.*

Proof. This has been proven by Brühl in [4, Lemma 3.5]. ∎

We can now prove our main theorems.

Proof of Theorems 2.1 *and* 2.2. Using Lemma 2.7, it follows from Lemma 2.6 that

$$\mathcal{R}\left(|\Im\left(\alpha_\omega \Lambda_\omega\right)|^{1/2}\right) = \mathcal{R}(L), \quad \text{resp.,} \quad \mathcal{R}\left(|\Re\left(\sigma_0^\omega \Lambda_\omega - \sigma_0^\tau \Lambda_\tau\right)|^{1/2}\right) = \mathcal{R}(L).$$

Hence, the assertions follow from Lemma 2.8. ∎

3. Numerical examples. We tested our method numerically and compared it to the conventional factorization method for static (zero frequency) electrical impedance tomography using exact and inexact reference measurements. B is the two-dimensional unit-disk. The inclusions are two circles centered in $(0.4, 0.2)$ and $(-0.6, 0)$ with radii 0.3 and 0.2. For the complex conductivity at a nonzero frequency ω, we use the values of the first example from Jain et al. in [22]. The background conductivity is $\sigma_0^\omega := 0.3 + 0.1\mathrm{i}$ and inside the inclusions Ω we set this value to $\sigma^\omega|_\Omega := 0.1 + 0.1\mathrm{i}$, i.e., $\sigma_\Omega^\omega := -0.2$. To compare our method with the original factorization method we use $\tau = 0$ as the second frequency and set the imaginary part of the conductivity to zero for that case, i.e., $\sigma_0 := 0.3$ and $\sigma_\Omega := -0.2$. (Consistent with the introduction we omit the index τ for the zero frequency case.) Then

$$\frac{\sigma_\Omega^\omega}{\sigma_0^\omega} = -0.6 + 0.2\mathrm{i} \quad \text{and} \quad \frac{\sigma_\Omega}{\sigma_0} = -\frac{2}{3},$$

so that the assumptions of both Theorems 2.1 and 2.2 are fulfilled. (This also follows from Remark 2.3 as $\tau = 0$ and only the conductivity differs in the inclusions.)

On ∂B we apply

$$\left\{ \frac{1}{\sqrt{\pi}} \sin(n\phi), \; \frac{1}{\sqrt{\pi}} \cos(n\phi) \;\middle|\; n = 1, \ldots, 128 \right\}$$

as input currents, where (r, ϕ) denotes the polar coordinates with respect to the origin.

We use the notation Λ_ω for the NtD operator at the frequency ω and Λ for the corresponding operator at zero frequency (both for the setting with the inclusion Ω). For the original factorization method we also need the reference operator at zero frequency without inclusion Λ_0, i.e., the one corresponding to constant real conductivity $\sigma_0 = 0.3$ throughout B. Accordingly, we denote the corresponding potentials by u, u_ω and u_0.

We calculate these potentials separately using the commercial finite element software Comsol and expand their boundary values in the aforementioned trigonometric basis, which gives us discrete approximations $\tilde{\Lambda}_\omega, \tilde{\Lambda}, \tilde{\Lambda}_0 \in \mathbb{C}^{256\times 256}$. Consistent with our theoretical results in section 2 we describe the applied currents as continuous functions (the so-called continuum model of EIT) and do not study more realistic electrode models in our numerical examples. Also note that we do not directly calculate the difference $\tilde{\Lambda} - \tilde{\Lambda}_0$ as in [13] or $\Im(\sigma_0^\omega \tilde{\Lambda}_\omega)$, resp., $\Re(\sigma_0\tilde{\Lambda} - \sigma_0^\omega \tilde{\Lambda}_\omega)$ in an analogous manner. Though such a direct calculation of the differences leads to a higher precision in the simulated forward data, we refrained from it in order to be able to simulate independent measurement and shape errors on each of the measurement operators.

The range criteria

$$z \in \Omega \quad \text{ if and only if } \quad \Phi_z|_{\partial B} \in \mathcal{R}\left(A^{1/2}\right)$$

with $A = |\Im(\sigma_0^\omega \Lambda_\omega)|$ (see Theorem 2.1), $A = |\Re(\sigma_0\Lambda - \sigma_0^\omega \Lambda_\omega)|$ (see Theorem 2.2) or $A = |\Lambda - \Lambda_0|$ (the conventional factorization method, see Brühl [4, Theorem 3.1]) are implemented as in [13]. For the reader's convenience we repeat the description here. Let

$$Av_k = \lambda_k v_k, \qquad k \in \mathbb{N},$$

be the spectral decomposition of the operator A, which is in all three cases compact, self-adjoint, injective, and positive. $\{v_k\} \subset L^2_\diamond(\partial B)$ is an orthonormal basis of eigenfunctions with eigenvalues $\{\lambda_k\} \subset \mathbb{R}$ (sorted in decreasing order). The Picard criterion yields that

$$\Phi_z|_{\partial B} \in \mathcal{R}(A^{1/2})$$

if and only if

$$f(z) := \frac{1}{\|\Phi_z|_{\partial B}\|^2_{L^2(\partial B)}} \sum_{k=1}^{\infty} \frac{|(\Phi_z|_{\partial B}, v_k)_{L^2(\partial B)}|^2}{\lambda_k} < \infty.$$

Using a singular value decomposition of the discrete approximation $\tilde{A} \in \mathbb{C}^{256\times 256}$ ($\tilde{A} = |\Im(\sigma_0^\omega \tilde{\Lambda}_\omega)|$, $\tilde{A} = |\Re(\sigma_0\tilde{\Lambda} - \sigma_0^\omega \tilde{\Lambda}_\omega)|$, or $\tilde{A} = |\tilde{\Lambda} - \tilde{\Lambda}_0|$),

$$\tilde{A}\tilde{v}_k = \tilde{\lambda}_k \tilde{u}_k, \qquad \tilde{A}^* \tilde{u}_k = \tilde{\lambda}_k \tilde{v}_k, \qquad k = 1, \ldots, 128,$$

with nonnegative $\{\tilde{\lambda}_k\} \subset \mathbb{R}$ (sorted in decreasing order) and orthonormal bases $\{\tilde{u}_k\}, \{\tilde{v}_k\} \subset \mathbb{C}^{256}$, we approximate the function $f(z)$ by

$$\tilde{f}(z) := \sum_{k=1}^{m} \frac{|\tilde{\Phi}_z^* \tilde{v}_k|^2}{\tilde{\lambda}_k} \Big/ \sum_{k=1}^{m} |\tilde{\Phi}_z^* \tilde{v}_k|^2,$$

where $\tilde{\Phi}_z \in \mathbb{C}^{256}$ contains the Fourier coefficients of $\Phi_z|_{\partial B}$, which for the two-dimensional unit circle can be written as (cf., e.g., Brühl [4]),

$$\Phi_z(x) = \frac{1}{\pi}\frac{(z-x)\cdot d}{|z-x|^2} \quad \text{for all } x \in \partial B.$$

m is the number of singular values that are reasonable approximations $\tilde{\lambda}_k \approx \lambda_k$. To estimate m we plot the (normalized) singular values $(\tilde{\lambda}_k)_k$ in a semilogarithmic scale; cf. the left column of Figure 3.1, where this is done for our three different choices for A. Typically, the eigenvalues show an exponential decay that stops rather abruptly due to the presence of errors in our simulated data. In our experiments we manually pick the level where this stop occurs (marked by a dashed line in our eigenvalue plots) and use only the singular values $(\tilde{\lambda}_k)_k$ above this level.

To obtain a numerical criterion telling whether a point z belongs to the unknown inclusion Ω or not, one now has to decide if the infinite sum $f(z)$ attains the value ∞ by using the approximate value $\tilde{f}(z)$, which is always finite. Thus, a threshold $C_\infty > 0$ is needed to distinguish points with *large* values $\tilde{f}(z) \geq C_\infty$ from those with *small* values $\tilde{f}(z) < C_\infty$. A reconstruction of Ω is then obtained by evaluating $\tilde{f}(z)$ on a grid of points $\{z_n\} \subset B$ and saying that all points with $\tilde{f}(z_n) < C_\infty$ belong to the inclusion. Choosing different threshold values C_∞ corresponds to choosing different level contours of $\tilde{f}(z)$ or, equivalently, of a monotone function of $\tilde{f}(z)$.

In our numerical experiments, we plot the indicator function

$$\mathrm{Ind}(z) := \Big(\log\big(1+\tilde{f}(z)\big)\Big)^{-1} \tag{3.1}$$

on an equidistant grid $\{z_n\} \subset B$, as well as the contour of $\tilde{f}$ that fits best to the true boundary of the inclusion $\partial\Omega$. Note that we choose this optimal contour line in order to compare optimal results for our method with optimal results for the original method. In practice, the choice of a contour line of $\tilde{f}$ has to be done on a heuristic basis or using additional information, e.g., about the size of the inclusion.

3.1. Detecting inclusions without reference measurements. Figure 3.1 shows the reconstructions that we obtain for $A = |\Im(\sigma_0^\omega \Lambda_\omega)|$ (top row), $A = |\Re(\sigma_0 \Lambda - \sigma_0^\omega \Lambda_\omega)|$ (middle row), and $A = |\Lambda - \Lambda_0|$ (bottom row). The left column shows the (normalized) singular values of A and the trust level marked by a dashed line, the middle column shows the indicator function, and the right column shows the optimal contour line of it (chosen with knowledge of the true inclusions). The true boundary of the inclusions $\partial\Omega$ is plotted with a dashed line in the middle and right columns.

The reconstructions are of similar good quality. For this case of exact simulated data it does not seem to matter whether only measurements at a single nonzero frequency are being used (top row), nonzero frequency measurements are combined with zero frequency measurements (middle row), or zero frequency measurements are combined with reference measurements (bottom row).

In addition to using unperturbed simulated measurements, we also tested the method after adding 0.1% relative noise to the measurement matrix $\tilde{\Lambda}_\omega$, resp., $\tilde{\Lambda}$. More precisely, we generate an error matrix E of the same size as the measurements with uniformly distributed real and imaginary parts of the entries between -1 and 1. E is then scaled to the noise level with respect to its spectral norm and added to the respective measurement operator. (Of course, different errors are added to $\tilde{\Lambda}_\omega$ and $\tilde{\Lambda}$.) We also compare this with the results obtained with the original factorization

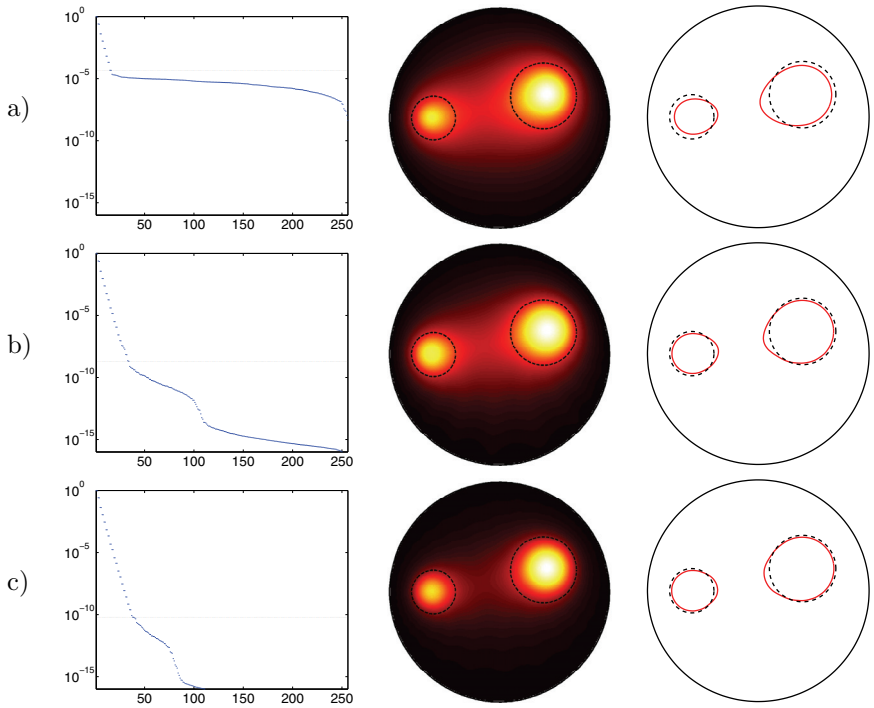

FIG. 3.1. *Numerical results for exact data: singular values (left column), indicator function (middle column), and its optimal contour (right column, chosen with knowledge of the true inclusions) for* (a) *single-frequency data,* (b) *frequency-difference data, and* (c) *static data compared with reference data.*

method, i.e., using $\tilde{\Lambda} - \tilde{\Lambda}_0$, where we take the noisy version of $\tilde{\Lambda}$ but not of $\tilde{\Lambda}_0$. The corresponding reconstructions are shown in Figure 3.2, which is organized in the same way as Figure 3.1.

The reconstructions using $A = |\Im(\sigma_0^\omega \Lambda_\omega)|$ in the top row and $A = |\Re(\sigma_0 \Lambda - \sigma_0^\omega \Lambda_\omega)|$ in the middle row seem to be more effected by the noise than those using $A = |\Lambda - \Lambda_0|$ in the bottom row. This can be explained by the fact that all three choices for A contain differences of the measurement operators Λ_ω, Λ, or Λ_0, which are much smaller than the measurement operators itself. Thus, the noise on the measurement operators is amplified in these differences. In our example we have that

$$\|\Im(\sigma_0^\omega \tilde{\Lambda}_\omega)\| \approx 0.06 \|\sigma_0^\omega \tilde{\Lambda}_\omega\|,$$

$$\|\Re(\sigma_0 \tilde{\Lambda} - \sigma_0^\omega \tilde{\Lambda}_\omega)\| \approx 0.03 \|\sigma_0 \tilde{\Lambda}\| \approx 0.03 \|\sigma_0 \tilde{\Lambda}\|,$$

$$\|\tilde{\Lambda} - \tilde{\Lambda}_0\| \approx 0.14 \|\tilde{\Lambda}\| \approx 0.16 \|\tilde{\Lambda}_0\|,$$

so that the noise amplification is highest in the middle row and lowest in the bottom row, which fits well to the different quality of the reconstruction. Note that this amount of noise amplification depends on the inclusions' contrast to the background conductivity and, though we have not thoroughly investigated this question, different numerical examples did not indicate that one choice of A is generally more robust to noise than another.

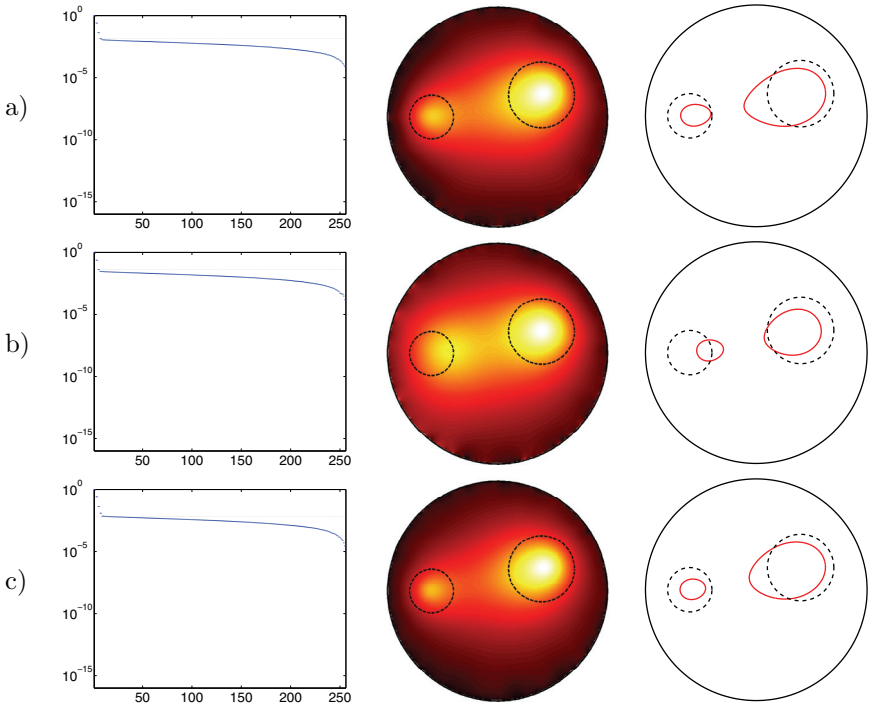

FIG. 3.2. *Numerical reconstructions for data containing* 0.1% *relative noise: singular values (left column), indicator function (middle column), and its optimal contour (right column, chosen with knowledge of the true inclusions) for* (a) *single-frequency data,* (b) *frequency-difference data, and* (c) *static data compared with reference data.*

3.2. Sensitivity to body shape errors. We also compared our method to the conventional factorization method in a setting where there are some boundary geometry errors between the computational domain of the forward model and that of the true body. To that end we replaced B by an ellipse with halfaxes $1+\delta$ and $1/(1+\delta)$ in the calculation of the forward data. Everything else remained unchanged to simulate the case where this ellipse is wrongly assumed to be the unit circle.

We used $\delta = 5\%$ and show in the first row of Figure 3.3 the reconstruction obtained from $A = |\Im(\sigma_0^\omega \Lambda_\omega)|$ and in the second row those obtained with $A = |\Re(\sigma_0 \Lambda - \sigma_0^\omega \Lambda_\omega)|$. As we explained in the introduction, for the conventional factorization method, using $A = |\Lambda - \Lambda_0|$, the effect of body shape errors strongly depends on whether the reference operator Λ_0 is experimentally obtainable or numerically simulated (resp., in easy cases, calculated analytically). In the first case, Λ_0 correctly corresponds to measurements at an ellipse (which the body really is), while in the latter case, it corresponds to a circle (which we wrongly assume the body to be). The resulting reconstructions are shown in the third and forth row of Figure 3.3.

As we expected, systematic body shape errors have a greater effect on the reconstructions when the measurement operators belong to a different geometry, as is the case for the conventional factorization method with simulated reference data, shown in the bottom row. However, also using only measurements at a single, nonzero frequency, i.e., $A = |\Im(\sigma_0^\omega \Lambda_\omega)|$ in the top row, seems to be similarly effected. If two different kinds of measurements are taken at the same body, the reconstructions improve. It does not seem to matter much whether these two are measurements at a

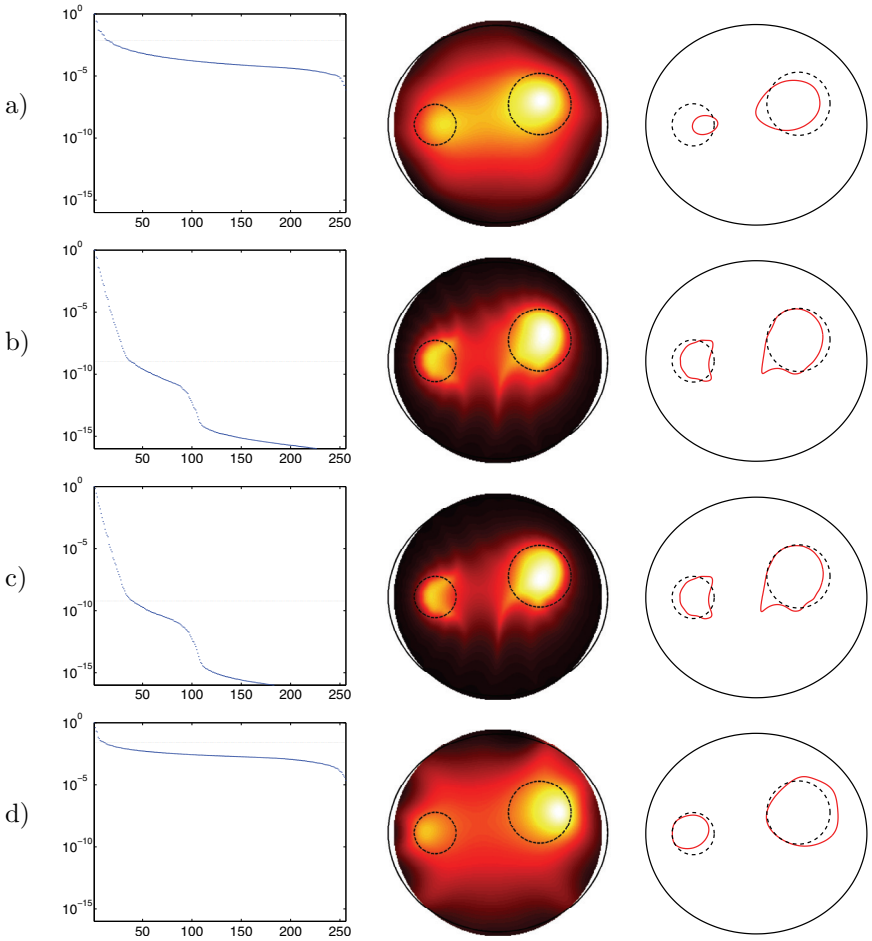

FIG. 3.3. *Numerical reconstructions for data containing $\delta = 5\%$ body shape errors: singular values (left column), indicator function (middle column), and its optimal contour (right column, chosen with knowledge of the true inclusions) for* (a) *single-frequency data,* (b) *frequency-difference data,* (c) *static data compared with reference data for the correct body shape, and* (d) *static data compared with reference data for the assumed (incorrect) body shape.*

nonzero and at zero frequency ($A = |\Re(\sigma_0\Lambda - \sigma_0^\omega\Lambda_\omega)|$ in the second row) or zero frequency measurements with and without inclusion ($A = |\Lambda - \Lambda_0|$ in the third row).

Figure 3.4, which is organized in the same way as Figure 3.3, shows the reconstructions that we obtained for an ellipse with halfaxes $1+\delta$ and $1/(1+\delta)$ for $\delta = 10\%$. Even for this rather large amount of errors in the estimated body shape the reconstructions are quite reasonable if frequency-difference measurements (second row) or the conventional factorization method is used with reference measurements belonging to the exact (elliptical) body shape (third row). If measurements at only a single, nonzero frequency are used (top row), the reconstruction gets highly blurred. The conventional method with reference measurements that are simulated for the assumed (incorrect) body shape (bottom row) performs even worse and leads to strong artifacts.

The results numerically verify that our new variant of the factorization method with frequency-difference data is much more robust against body shape errors than

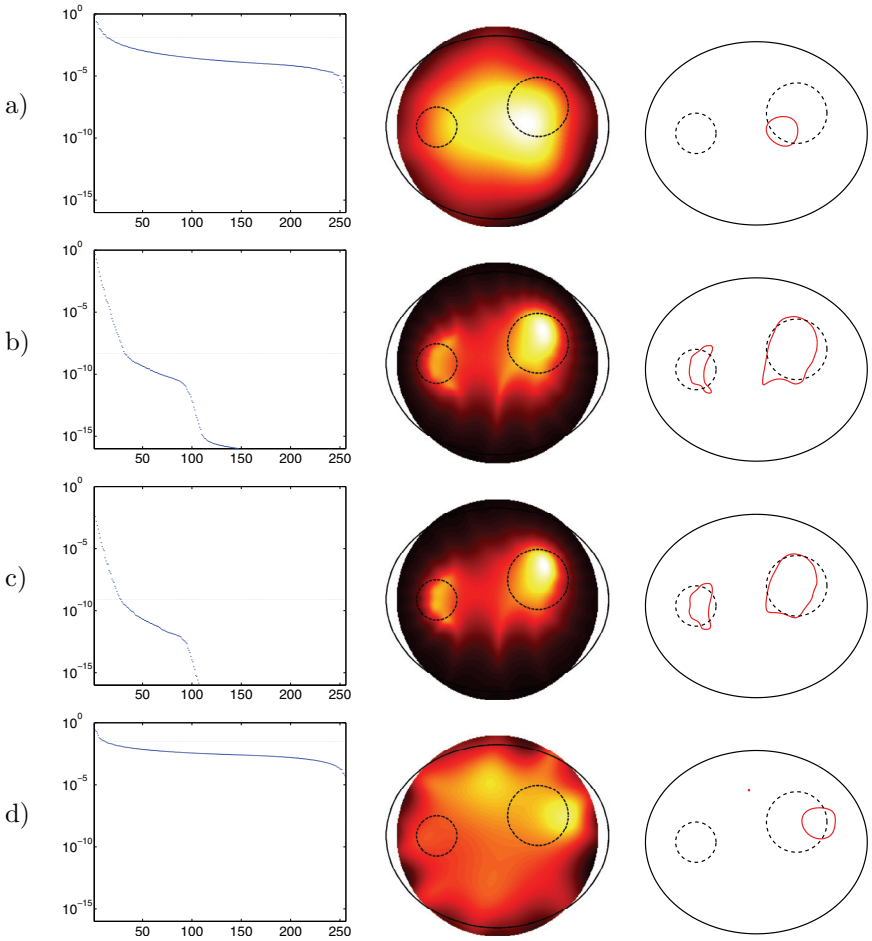

FIG. 3.4. *Numerical reconstructions for data containing $\delta = 10\%$ body shape errors: singular values (left column), indicator function (middle column), and its optimal contour (right column, chosen with knowledge of the true inclusions) for* (a) *single-frequency data,* (b) *frequency-difference data,* (c) *static data compared with reference data for the correct body shape, and* (d) *static data compared with reference data for the assumed (incorrect) body shape.*

using the conventional method with simulated (or analytically calculated) reference data. Actually, the reconstructions using frequency-difference data seem to be of equally good quality and robustness as those that one would obtain with correct reference measurements (which are usually not available in practice).

3.3. Unknown background conductivity. Though our new variant of the factorization method works without reference measurements, it still requires the knowledge of the constant conductivity value of the background. We now describe a heuristic approach with which the algorithm can also be applied to an unknown background conductivity.

Roughly speaking, we expect that fast spatial variations in the applied currents on ∂B lead to higher electric currents close to ∂B, while the electric effect of slowly spatially varying currents penetrates deeper into B (see [12] for a detailed study of how to create potentials with localized electrical energy). We also expect that the

eigenfunctions of our compact measurement operators Λ^ω, resp., Λ, are functions containing increasingly high oscillations. Thus, the eigenvalues will mostly depend on the conductivity close to ∂B, i.e., the background conductivity, σ_0^ω, resp., σ_0.

The multiplication of Λ_ω with the background value σ_0^ω can be regarded as a simple change of units that sets this background conductivity value to the real value 1. Thus, we expect the eigenvalues of $\sigma_0^\omega \Lambda_\omega$ to mostly lie close to the real axis, and so the eigenvalues of Λ_ω will lie close to a straight line through the origin whose angle with the real axis is minus the phase of σ_0^ω.

To determine the range of $|\Im(\sigma_0^\omega \Lambda_\omega)|^{1/2}$, it suffices to estimate this phase of σ_0^ω. We do this by choosing the median α of the set

$$\left\{ -\frac{\Im(\tilde{\lambda}_j^\omega)}{\Re(\tilde{\lambda}_j^\omega)} \ : \ j = 1, 2, \dots \right\}$$

using all available eigenvalues $\tilde{\lambda}_j^\omega$ of $\tilde{\Lambda}_\omega$. Instead of $A = |\Im(\sigma_0^\omega \Lambda_\omega)|$ we then use $A = |\Im((1 + \alpha \mathrm{i})\Lambda_\omega)|$ in our algorithm.

To estimate the range of $|\Re(\sigma_0 \Lambda - \sigma_0^\omega \Lambda_\omega)|^{1/2}$ we proceed analogously and estimate the quotient of σ_0^ω and σ_0 by the median β of the set

$$\left\{ \frac{\tilde{\lambda}_j}{\tilde{\lambda}_j^\omega} \ : \ j = 1, 2, \dots \right\}$$

using all available eigenvalues $\tilde{\lambda}_j^\omega$ of $\tilde{\Lambda}_\omega$ and $\tilde{\lambda}_j$ of $\tilde{\Lambda}$. Then we use $A = |\Re(\Lambda - \beta \Lambda_\omega)|$ in our algorithm.

Figure 3.5 shows the reconstructions that we obtained with this approach for our numerical example. The columns are organized as in Figures 3.1–3.4. The first two rows show the reconstructions obtained with $A = |\Im((1 + \alpha \mathrm{i})\Lambda_\omega)|$ and $A = |\Re(\Lambda - \beta \Lambda_\omega)|$ and the last two rows show the according reconstructions after adding 0.1% of relative noise as in subsection 3.1. The reconstructions show almost no visual difference to those obtained with the exact background conductivity values in subsection 3.1.

Though this is not covered by the theory presented in section 2, it seems plausible that the above approach can also be applied to cases where the unknown background is slightly inhomogeneous. In our final example we test this numerically for the factorization method with frequency-difference data. We multiply the complex background conductivity used in the previous examples with the slightly oscillating function

$$1 + 0.05 \cos(4\pi x) \sin(8\pi y).$$

In order to retain the conductivity jump only in the real part, we also multiply the imaginary part of the conductivity inside the inclusions with this function. Figure 3.6 shows the resulting real part (left picture) and the imaginary part (right picture) of σ^ω. As in the previous examples, we assume that the static conductivity σ has the same real part as σ^ω and that it has zero imaginary part.

We also added $\delta = 5\%$ body shape error as in subsection 3.2 and 0.05% relative noise as in subsection 3.1. Figure 3.7 shows the reconstruction that we obtain from using frequency-difference data $A = |\Re(\Lambda - \beta \Lambda_\omega)|$, where the constant $\beta \in \mathbb{C}$ is estimated from the data as explained above.

The reconstruction are comparable to those obtained with knowledge of the exact body shape, known constant background, and 0.1% relative noise in subsection 3.1. This suggests that the method can indeed be applied to the practically relevant case of an unknown inhomogeneous background that is only known to be "almost constant."

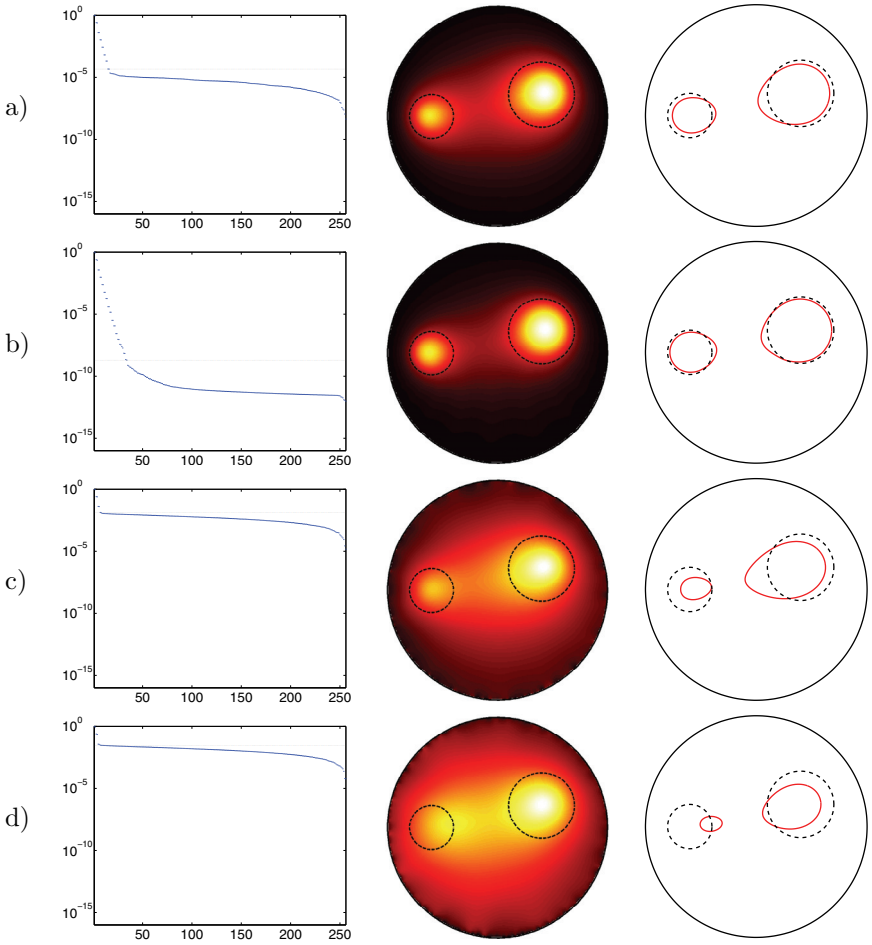

FIG. 3.5. *Numerical reconstructions for an unknown, but constant, background conductivity: singular values (left column), indicator function (middle column), and its optimal contour (right column, chosen with knowledge of the true inclusions) for* (a) *exact single-frequency data,* (b) *exact frequency-difference data,* (c) *single-frequency data containing* 0.1% *relative noise, and* (d) *frequency-difference data containing* 0.1% *relative noise.*

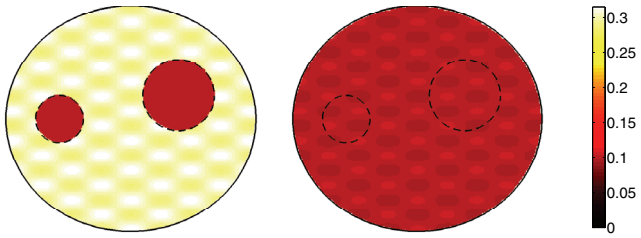

FIG. 3.6. *Real and imaginary part of the conductivity describing inclusions in a slightly inhomogeneous background.*

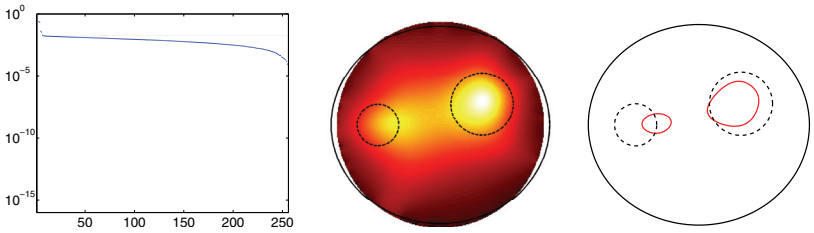

FIG. 3.7. *Numerical reconstructions for an unknown, slightly inhomogeneous background conductivity using frequency-difference data containing $\delta = 5\%$ body shape errors and 0.05% relative noise: singular values (left column), indicator function (middle column), and its optimal contour (right column, chosen with knowledge of the true inclusions).*

4. Conclusions. We have developed a new variant of the factorization method that can be used on single-frequency and on frequency-difference measurements in electrical impedance tomography and that does not require reference measurements at an inclusion-free body, which are usually not available in practice. Our new variant with single-frequency measurements delivers comparable results to using the conventional method with simulated reference data and thus eliminates one of the main computational efforts in applying the method. An even greater advantage is achieved by using frequency-difference measurements. Not only do we save the computational effort of simulating reference measurements, but our new results show the same performance in the presence of body shape errors that one would otherwise obtain from reference measurements at the correct (unknown) body shape. This greatly improves the stability of the method with respect to such unavoidable systematic errors, so that the application of the method in frequency-difference EIT systems seems very promising.

REFERENCES

[1] H. AMMARI, R. GRIESMAIER, AND M. HANKE, *Identification of small inhomogeneities: Asymptotic factorization*, Math. Comp., 76 (2007), pp. 1425–1448.
[2] H. AMMARI AND J. K. SEO, *An accurate formula for the reconstruction of conductivity inhomogeneities*, Adv. in Appl. Math., 30 (2003), pp. 679–705.
[3] N. BOURBAKI, *Elements of Mathematics, Topological Vector Spaces*, Chapters 1–5, Springer-Verlag, Berlin, 2003.
[4] M. BRÜHL, *Explicit characterization of inclusions in electrical impedance tomography*, SIAM J. Math. Anal., 32 (2001), pp. 1327–1341.
[5] M. BRÜHL AND M. HANKE, *Numerical implementation of two noniterative methods for locating inclusions by impedance tomography*, Inverse Problems, 16 (2000), pp. 1029–1042.
[6] M. BRÜHL, M. HANKE, AND M. S. VOGELIUS, *A direct impedance tomography algorithm for locating small inhomogeneities*, Numer. Math., 93 (2003), pp. 635–654.
[7] R. DAUTRAY AND J. L. LIONS, *Mathematical Analysis and Numerical Methods for Science and Technology—Volume 2: Functional and Variational Methods*, Springer-Verlag, Berlin, 2000.
[8] H. ECKEL AND R. KRESS, *Nonlinear integral equations for the inverse electrical impedance problem*, Inverse Problems, 23 (2007), pp. 475–491.
[9] K. ERHARD AND R. POTTHAST, *The point source method for reconstructing an inclusion from boundary measurements in electrical impedance tomography and acoustic scattering*, Inverse Problems, 19 (2003), pp. 1139–1157.
[10] F. FRÜHAUF, B. GEBAUER, AND O. SCHERZER, *Detecting interfaces in a parabolic-elliptic problem from surface measurements*, SIAM J. Numer. Anal., 45 (2007), pp. 810–836.
[11] B. GEBAUER, *The factorization method for real elliptic problems*, Z. Anal. Anwend., 25 (2006), pp. 81–102.
[12] B. GEBAUER, *Localized potentials in electrical impedance tomography*, Inverse Probl. Imaging,

2 (2008), pp. 251–269.
[13] B. Gebauer and N. Hyvönen, *Factorization method and irregular inclusions in electrical impedance tomography*, Inverse Problems, 23 (2007), pp. 2159–2170.
[14] M. Hanke and M. Brühl, *Recent progress in electrical impedance tomography*, Inverse Problems, 19 (2003), pp. S65–S90.
[15] M. Hanke, N. Hyvönen, and S. Reusswig, *Convex source support and its application to electric impedance tomography*, SIAM J. Imaging Sci., 1 (2008), pp. 364–378.
[16] M. Hanke and B. Schappel, *The factorization method for electrical impedance tomography in the half-space*, SIAM J. Appl. Math., 68 (2008), pp. 907–924.
[17] F. Hettlich and W. Rundell, *The determination of a discontinuity in a conductivity from a single boundary measurement*, Inverse Problems, 14 (1998), pp. 67–82.
[18] N. Hyvönen, *Complete electrode model of electrical impedance tomography: Approximation properties and characterization of inclusions*, SIAM J. Appl. Math., 64 (2004), pp. 902–931.
[19] N. Hyvönen, H. Hakula, and S. Pursiainen, *Numerical implementation of the factorization method within the complete electrode model of electrical impedance tomography*, Inverse Probl. Imaging, 1 (2007), pp. 299–317.
[20] T. Ide, H. Isozaki, S. Nakata, S. Siltanen, and G. Uhlmann, *Probing for electrical inclusions with complex spherical waves*, Comm. Pure Appl. Math., 60 (2007), pp. 1415–1442.
[21] K. Ito, K. Kunisch, and Z. Li, *Level-set function approach to an inverse interface problem*, Inverse Problems, 17 (2001), pp. 1225–1242.
[22] H. Jain, D. Isaacson, P. M. Edic, and J. C. Newell, *Electrical impedance tomography of complex conductivity distributions with noncircular boundary*, IEEE Trans. Biomedical Engineering, 44 (1997), pp. 1051–1060.
[23] H. Kang, J. K. Seo, and D. Sheen, *The inverse conductivity problem with one measurement: Stability and estimation of size*, SIAM J. Math. Anal., 28 (1997), pp. 1389–1405.
[24] A. Kirsch, *Characterization of the shape of a scattering obstacle using the spectral data of the far field operator*, Inverse Problems, 14 (1998), pp. 1489–1512.
[25] A. Kirsch, *The factorization method for a class of inverse elliptic problems*, Math. Nachr., 278 (2005), pp. 258–277.
[26] A. Kirsch and N. Grinberg, *The Factorization Method for Inverse Problems*, Oxford Lecture Ser. Math. Appl. 36, Oxford University Press, Oxford, 2008.
[27] O. Kwon, J. K. Seo, and J. R. Yoon, *A real-time algorithm for the location search of discontinuous conductivities with one measurement*, Comm. Pure Appl. Math., 55 (2002), pp. 1–29.
[28] O. Kwon, J. R. Yoon, J. K. Seo, E. J. Woo, and Y. G. Cho, *Estimation of anomaly location and size using electrical impedance tomography*, IEEE Trans. Biomed. Eng., 50 (2003), pp. 89–96.
[29] A. Lechleiter, N. Hyvönen, and H. Hakula, *The factorization method applied to the complete electrode model of impedance tomography*, SIAM J. Appl. Math., 68 (2008), pp. 1097–1121.
[30] A. I. Nachman, L. Päivärinta, and A. Teirilä, *On imaging obstacles inside inhomogeneous media*, J. Funct. Anal., 252 (2007), pp. 490–516.
[31] T. I. Oh, J. Lee, J. K. Seo, S. W. Kim, and E. J. Woo, *Feasibility of breast cancer lesion detection using a multi-frequency trans-admittance scanner (tas) with* 10 *hz to* 500 *khz bandwidth*, Physiol. Meas., 28 (2007), pp. S71–S84.
[32] J. K. Seo, J. Lee, H. Zribi, S. W. Kim, and E. J. Woo, *Frequency-difference electrical impedance tomography (fdEIT): Algorithm development and feasibility study*, Physiol. Meas., 29 (2008), pp. 929–944.